



# X-ray phase-contrast microtomography of soft tissues using a compact laboratory system with two-directional sensitivity

CARLOS NAVARRETE-LEÓN,<sup>1</sup> ADAM DOHERTY,<sup>1</sup> SAVVAS SAVVIDIS,<sup>1</sup> MATTIA F. M. GERLI,<sup>2,3</sup> GIOVANNI PIREDDA,<sup>4</sup> ALBERTO ASTOLFO,<sup>1</sup> DAVID BATE,<sup>1,5</sup> SILVIA CIPICCIA,<sup>1</sup> CHARLOTTE K. HAGEN,<sup>1</sup> ALESSANDRO OLIVO,<sup>1</sup> AND MARCO ENDRIZZI<sup>1,\*</sup>

<sup>1</sup>Department of Medical Physics and Biomedical Engineering, University College London, Gower Street, London, WC1E 6BT, UK

<sup>2</sup>UCL Division of Surgery and Interventional Science, Royal Free Hospital, Rowland Hill Street, London, NW3 2PF, UK

<sup>3</sup>Stem Cell and Regenerative Medicine Section, Great Ormond Street Institute of Child Health, University College London, London, WC1N 1EH, UK

<sup>4</sup>Research Center for Microtechnology, Vorarlberg University of Applied Sciences, Hochschulstr. 1, 6850, Dornbirn, Austria

<sup>5</sup>Nikon X-Tek Systems Ltd, Tring, Herts, HP23 4JX, UK

\*m.endrizzi@ucl.ac.uk

Received 7 February 2023; revised 18 May 2023; accepted 1 June 2023; published 30 June 2023

X-ray microtomography is a nondestructive, three-dimensional inspection technique applied across a vast range of fields and disciplines, ranging from research to industrial, encompassing engineering, biology, and medical research. Phase-contrast imaging extends the domain of application of x-ray microtomography to classes of samples that exhibit weak attenuation, thus appearing with poor contrast in standard x-ray imaging. Notable examples are low-atomic-number materials, like carbon-fiber composites, soft matter, and biological soft tissues. We report on a compact and cost-effective system for x-ray phase-contrast microtomography. The system features high sensitivity to phase gradients and high resolution, requires a low-power sealed x-ray tube, a single optical element, and fits in a small footprint. It is compatible with standard x-ray detector technologies: in our experiments, we have observed that single-photon counting offered higher angular sensitivity, whereas flat panels provided a larger field of view. The system is benchmarked against known-material phantoms, and its potential for soft-tissue three-dimensional imaging is demonstrated on small-animal organs: a piglet esophagus and a rat heart. We believe that the simplicity of the setup we are proposing, combined with its robustness and sensitivity, will facilitate accessing quantitative x-ray phase-contrast microtomography as a research tool across disciplines, including tissue engineering, materials science, and nondestructive testing in general.

Published by Optica Publishing Group under the terms of the [Creative Commons Attribution 4.0 License](https://creativecommons.org/licenses/by/4.0/). Further distribution of this work must maintain attribution to the author(s) and the published article's title, journal citation, and DOI.

<https://doi.org/10.1364/OPTICA.487270>

## 1. INTRODUCTION

X-ray microtomography has become an invaluable tool for the nondestructive volumetric imaging of samples for a wide variety of fields, ranging from medical sciences to metrology and manufacturing [1–3]. Despite continuous progress in x-ray microtomography technology, three-dimensional imaging of low-density samples, such as soft tissue specimens, remains challenging due to the weak x-ray attenuation contrast that is linked to low atomic number materials. X-ray phase-contrast microtomography (XPC $\mu$ T) can overcome this limitation by exploiting also the phase shift experienced by the wave when traversing the object for generating image contrast [4], thus extending the applicability of microtomography to a broader range of samples and disciplines.

The technology for x-ray phase-contrast imaging is more demanding in comparison to what is needed for conventional x-ray imaging, specifically in terms of the required spatial and temporal coherence of the radiation [4]. While synchrotron radiation

facilities can achieve high degrees of coherence, that is not often the case for laboratory-based systems, where the power density for x-ray generation is limited and a small footprint is required. In turn, this means that one has to choose between having a small or a powerful source, and working with monochromatic radiation often requires long exposure times. Many solutions have been identified and pursued over the past 25 years to overcome these limitations and facilitate the translation of x-ray phase-contrast imaging to a laboratory setting. Without compiling a complete history, here we summarize some of the milestones: microfocus source and crystal combination [5], free-space propagation with polychromatic radiation [6], Talbot–Lau interferometry [7–9], edge illumination [10,11], single-shot differential phase contrast and diffraction through spatial harmonic analysis [12], liquid metal jet sources [13], universal moiré effect [14], speckle-based imaging also in combination with liquid metal jet sources [15–18] and implicit tracking [19]; we refer to some excellent reviews on

the topic for a more comprehensive list and discussion [20–26]. Notable laboratory-based XPC $\mu$ T applications include imaging of soft-tissue specimens like lung [27,28], breast [29], heart [30], esophagus [31], brain [32], multimaterial phantoms [33–35], and for composites like carbon fiber-reinforced composite materials [36].

In this context, we have identified a solution for lab-XPC $\mu$ T that has minimum requirements on the experimental setup. Our approach is based on a low-power, fixed target and sealed x-ray tube; it requires a single optical element (modulator), and it is compatible with flat-panel detectors as well as with single-photon counters. All of these components are readily available and require a minimal amount of maintenance. The modulator is fabricated through laser ablation of a tungsten foil and requires positioning accuracy of approximately 5–10  $\mu$ m. The total length of the system is less than 1 m, making it one of the most compact for lab-XPC $\mu$ T. Our approach shares similarities with a Shack–Hartmann wavefront sensor and in our work, it evolved from one-directional to two-directional sensitivity of beam tracking [37,38]. It can also be viewed as a highly parallelized version of a single-probe scanning system [39]. We call this approach two-directional beam tracking (2DBT). This solution offers a compact, robust, and cost-effective way of producing multicontrast three-dimensional images of the inner structure of samples, without compromising on angular sensitivity.

## 2. MATERIALS AND METHODS

### A. Model

The core element of the imaging system [Fig. 1(a)] is the structured illumination, obtained by spatially modulating the amplitude of the radiation field before it reaches the sample. Structuring the illumination in two dimensions enables tracking small changes in the position of each probe, i.e., measuring refraction along two orthogonal directions. It redefines sampling and spatial resolution of the imaging system. Sampling is no longer governed by the detector pixel pitch; it is instead defined by the distance between apertures in the modulator. The spatial resolution is redefined as being equal to or better than the width of the apertures in the

modulator [40,41]. The main drawback of this approach is the sacrifice in flux available for imaging. We note, however, that this sacrifice does not affect dose efficiency because the radiation field is shaped before it reaches the sample. We also note that sampling is not necessarily limited by the pitch of the modulator: finer sampling can be achieved by recombining subsequent exposures, having moved either the modulator or the sample by a fraction of the pitch. We increase sampling by displacing the modulator by equally spaced subpitch increments. This requires a reference image for each modulator position; however, it preserves the conventional cone beam geometry and allows using standard three-dimensional reconstruction algorithms, even for the data sets acquired with higher sampling. Each probe is detected, and subsequently analyzed, independently. The x-ray intensity distribution of each probe is modeled through a series of convolutions,

$$I_0(x, y) = (S * M * \text{PSF})(x, y), \quad (1)$$

where  $*$  denotes the two-dimensional convolution operator,  $S$  is the source intensity distribution, geometrically scaled by  $-1 + (z_{sm} + z_{mo} + z_{od})/z_{sm}$ ,  $M$  is the transmission of the modulator (unity over a circle representing the aperture and zero elsewhere) geometrically scaled by  $(z_{sm} + z_{mo} + z_{od})/z_{sm}$ , and PSF is the detector point spread function. Referring to Fig. 1(a),  $z_{sm}$  is the distance between the source and the modulator,  $z_{mo}$  is the distance between the modulator and the axis of rotation, and  $z_{od}$  is the distance between the axis of rotation and the detector.

When a sample is in place, the intensity distribution of each probe is attenuated and shifted by the local properties of the sample,

$$I(x, y) = t I_0(x - \Delta x, y - \Delta y), \quad (2)$$

where  $t$  is the transmission through the sample (at the position of the probe) and  $\Delta x$  and  $\Delta y$  are the probe displacements on the detector plane due to the refraction induced by the sample. These shifts are measured by comparing the probe intensity distributions with and without the object [Fig. 1(b)]. The transmission is calculated as the ratio of the total intensity in the probe,

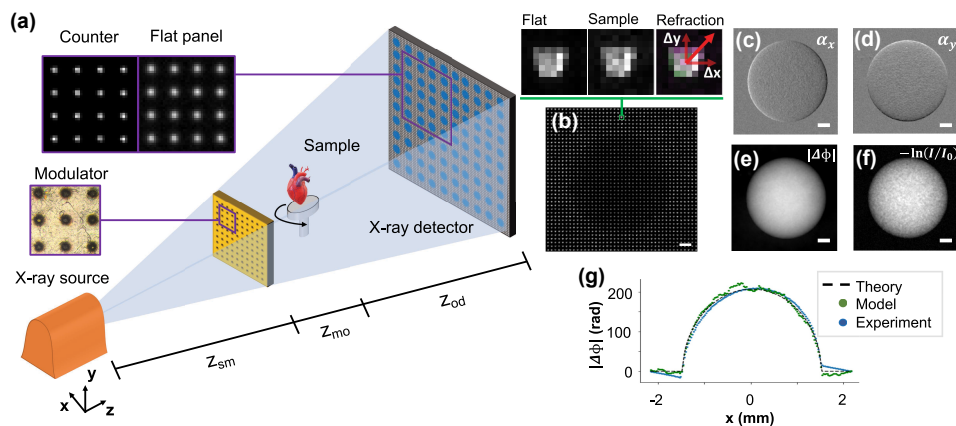


**Fig. 1. System's setup and working principle.** (a) Schematic of the laboratory set-up, including a sealed microfocus x-ray tube, the modulator, sample stage, and x-ray detector; (b) experimental image of a PMMA calibration sphere with an inset comparing beamlets without and with the sample in place; (c)–(d) effects of the presence of the sample are barely detectable by eye inspection; however, the dedicated data analysis algorithm reliably extracts refraction images. These are subsequently integrated leading to (e) phase images that offer superior signal-to-noise ratio to the (f) standard attenuation-contrast image. The refraction images are retrieved with a subpixel cross-correlation algorithm; we observe good agreement between the phase shift expected from theory, obtained through the numerical simulation, and from experimental data. All scale bars are 500  $\mu$ m.

$$t = \frac{\sum I(x, y)}{\sum I_0(x, y)}, \quad (3)$$

where sum operates over all the pixels illuminated by a single probe [Fig. 1(b), zoom-ins]. For the retrieval of the displacements  $\Delta x$  and  $\Delta y$ , we used a subpixel cross-correlation algorithm [42]. These displacements are related to the refraction angle and to the object-to-detector distance,  $z_{od}$ , by

$$\alpha_x(x, y) = \tan^{-1} \left( \frac{\Delta x}{z_{od}} \right), \quad \alpha_y(x, y) = \tan^{-1} \left( \frac{\Delta y}{z_{od}} \right). \quad (4)$$

By linking the two refraction images to the orthogonal gradients of the phase shift (Fig. 1, panels *c* and *d*) we obtain

$$\alpha_x(x, y) = \frac{1}{k} \Delta \Phi_x(x, y), \quad \alpha_y(x, y) = \frac{1}{k} \Delta \Phi_y(x, y), \quad (5)$$

where  $k$  is the wavenumber.

The phase shift of the wavefront  $\Delta \Phi(x, y)$  [Fig. 1(e)] can be obtained from the following expression:

$$\Delta \Phi(x, y) = \mathcal{F}^{-1} \left[ \frac{\mathcal{F}[\Delta \Phi_x + i \Delta \Phi_y](u, v)}{2\pi i(u + iv)} \right](x, y), \quad (6)$$

where  $(u, v)$  represent the reciprocal space coordinates to  $(x, y)$ . This expression can be obtained using the Fourier derivative theorem as follows [43]:

$$\begin{aligned} & \mathcal{F}[\Delta \Phi_x + i \Delta \Phi_y](u, v) \\ &= \int_{-\infty}^{\infty} \int_{-\infty}^{\infty} (\Delta \Phi_x + i \Delta \Phi_y) \cdot e^{-2\pi i(ux+vy)} dx dy \\ &= 2\pi i(u + iv) \cdot \mathcal{F}[\Delta \Phi(x, y)]. \end{aligned} \quad (7)$$

A better signal-to-noise ratio can be seen by direct visual comparison with the attenuation-image contrast of the same phantom [Fig. 1(f)]. The retrieved quantities  $t$  and  $\Delta \Phi$  are line integrals along the photon path of two physical properties of the sample, the linear attenuation coefficient ( $\mu$ ) and the real part of the refractive index ( $\delta$ ),

$$-\ln t(x, y) = \int_o \mu(x', y', z') dz, \quad (8)$$

$$-\frac{\Delta \Phi(x, y)}{k} = \int_o \delta(x', y', z') dz. \quad (9)$$

These relationships allow one to obtain volumetric reconstructions of  $\mu$  and  $\delta$  from projections taken at different viewing angles using the standard algorithms for tomography.

## B. Experiments

The x-ray system features a fixed W-target microfocus Hamamatsu x-ray source (L12161-07), which we run at 40 kVp and 10 W. The modulators were manufactured with a laser ablation procedure from readily available 100- $\mu$ m-thick tungsten foils (Goodfellow). Two pitches, 50 and 100  $\mu$ m, were tested. The apertures have a conical shape with diameters of  $\sim 15$   $\mu$ m and  $\sim 30$   $\mu$ m in the front and back apertures, respectively; the narrower aperture was facing the source.

Three detectors were tested: i) Pixirad-2/PIXIE-III photon counter with a 650  $\mu$ m CdTe sensor (98% detection efficiency up to 50 keV), 62  $\mu$ m pixel pitch and a  $50 \times 32$  mm<sup>2</sup> active area; ii) MerlinX photon counter (Quantum Detectors) with a Medipix 3RX chip ( $256 \times 256$ ), a 500  $\mu$ m Si sensor and 55  $\mu$ m pixel pitch; and iii) Hamamatsu flat panel (C9732DK-11) with directly deposited CsI scintillator, 50  $\mu$ m pixel pitch and  $12 \times 12$  cm<sup>2</sup> active area. Single-photon-counting detectors were chosen in view of achieving the highest angular sensitivity, whereas the flat panel was employed to allow for a larger field of view.

The geometry was defined as follows:  $z_{sm} = (150, 150, 140)$  mm,  $z_{mo} = (30, 30, 25)$  mm, and  $z_{od} = (680, 580, 535)$  mm, for the Pixirad, MerlinX and Hamamatsu detectors, respectively.

To characterize the system and fine-tune the quantitative retrieval algorithm, a test phantom consisting of a poly(methyl methacrylate) (PMMA) calibration sphere (Goodfellow,  $\varnothing = 3.18 \pm 0.05$  mm) was used. For the experimental assessment of spatial resolution, we used a phantom composed of soda-lime glass microspheres (Fischer Scientific, monodisperse, 50  $\mu$ m diameter) deposited on a kapton substrate. The detector was the Pixirad with the 100  $\mu$ m-pitch modulator and noise threshold set at 10 keV. A total of  $16 \times 16$  frames were acquired for both phantoms, with a sampling step in both  $x$  and  $y$  directions of 6.25  $\mu$ m and 1 s exposure time per frame.

The angular sensitivity was quantified on planar images of a phantom composed of soda-lime glass microspheres (Fischer Scientific, monodisperse, 50  $\mu$ m diameter) embedded in wax and polyethylene foam. Images were acquired at  $4 \times 4$  positions, with  $x$  and  $y$  steps of 12.5  $\mu$ m. The detector was the MerlinX with the 50  $\mu$ m-pitch modulator and noise threshold set at 5 keV. For each step, 256 frames of 0.25 s exposure time were acquired to study the angular sensitivity as a function of exposure time. The angular sensitivity was measured in an area without the sample by calculating the mean and standard error of the standard deviation of the measured refraction angles [44], nine different windows of  $10 \times 10$  pixels each were used. This approach quantifies the dispersion of noise in the refraction image, in turn indicating what is the minimum refraction angle that would be detectable by an imaging system.

The ability of the system to measure  $\mu$  and  $\delta$  in three dimensions was assessed with a multimaterial phantom composed of three spheres (Goodfellow) in a plastic straw. The materials were polypropylene (PP), polystyrene (PS) and PMMA with diameters:  $\varnothing_{PP, PMMA} = 3.18 \pm 0.05$  mm,  $\varnothing_{PS} = 3.5 \pm 0.1$  mm. The detector was the Pixirad with the 100  $\mu$ m-pitch modulator and noise threshold set at 8 keV. We acquired 900 projections over  $360^\circ$  with 1 s exposure time per projection. A full rotation was acquired for each modulator position, giving a total of  $8 \times 8$  scans with sampling every 12.5  $\mu$ m in  $x$  and  $y$ .

The performance of the system for soft-tissue imaging was demonstrated with two animal-derived small organs; a heart and an esophagus, extracted from a 300 g Sprague–Dawley rat and a 3 kg piglet, respectively. The heart sample was obtained from the UCL Biological Services Unit (BSU), while the esophagus from piglets was procured from JSR Genetics Ltd, a Home Office-approved supplier. Animals were euthanized via Schedule 1 methods, and sample sizing has been implemented following the NC3R principles. The organs were prepared for imaging through paraformaldehyde (PFA) fixation, followed by critical point drying

(as described in previous work [31]). For the piglet esophagus, we acquired 900 equally spaced projections over  $360^\circ$  with 1 s exposure time using the Pixirad detector. The  $100\ \mu\text{m}$ -pitch modulator was stepped by  $12.5\ \mu\text{m}$  in  $x$  and  $y$  for a total of  $8 \times 8$  scans and an exposure time of  $900 \times 8 \times 8 \times 1\ \text{s} = 16\ \text{h}$ . For the rat heart, we acquired 2000 equally spaced projections over  $360^\circ$  with 1.2 s exposure time using the Hamamatsu flat panel. The  $50\ \mu\text{m}$ -pitch modulator was stepped  $4 \times 4$  times on a grid with  $12.5\ \mu\text{m}$  displacements in  $x$  and  $y$ . The total exposure time was  $2000 \times 4 \times 4 \times 1.2\ \text{s} = 10.7\ \text{h}$ .

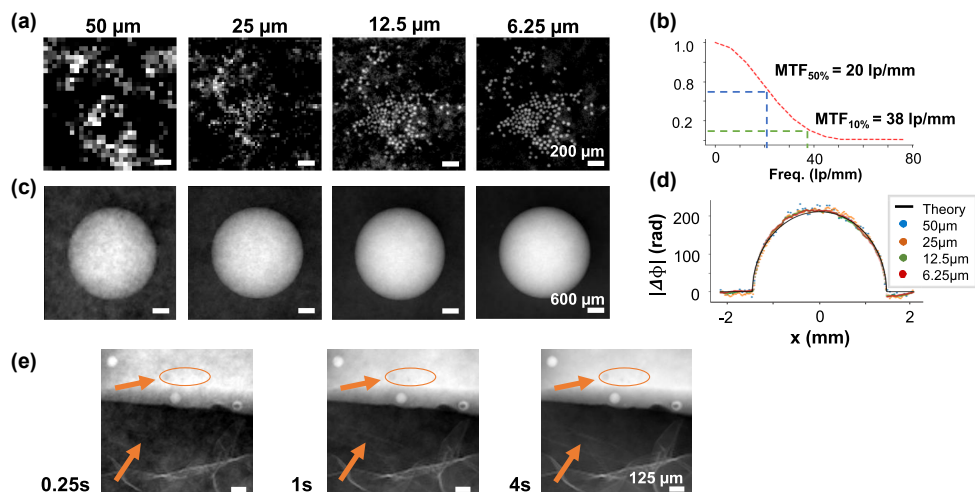
All reconstructions were performed using the Feldkamp–Davis–Kress algorithm implementation in CUDA of the Astra Toolbox [45]. The volume rendering presented in Fig. 5 were obtained using the Avizo software (Thermo Fischer Scientific).

### 3. RESULTS AND DISCUSSION

Figures 2(a) and 2(c) report the resolution phantom and the PMMA calibration sphere at different sampling steps, ranging from  $50$  to  $6.25\ \mu\text{m}$ . The positioning of the modulator has to be accurate and repeatable in comparison to these numbers, namely, approximately half of the aperture width, which is compatible with most micropositioning technologies. While the phase shift of a large object is correctly retrieved in all cases, the ability to represent finer details and distinguish between adjacent microspheres critically depends on the sampling step. The modulation transfer function (MTF) of the system at  $6.25\ \mu\text{m}$  sampling pitch is shown in Fig. 2(b), with 50% at  $20\ \text{lp/mm}$  and 10% at  $38\ \text{lp/mm}$ . The MTF was obtained as the Fourier transform of the PSF, which was experimentally evaluated against the images of a well-known object [46]. It matches well with the expectation from a real-space full width at half-maximum of  $16\ \mu\text{m}$ , comparable to the aperture size in the modulator. Figure 2(d) shows four line plots extracted from the phase images in panel 2(c) against the theoretically expected phase shift. There is good agreement between the phase shifts measured with different sampling steps and theory, with higher

noise linked to lower sampling. The decrease in noise that is linked to progressively finer sampling is also visible by visual comparison of the four images in panel 2(c).

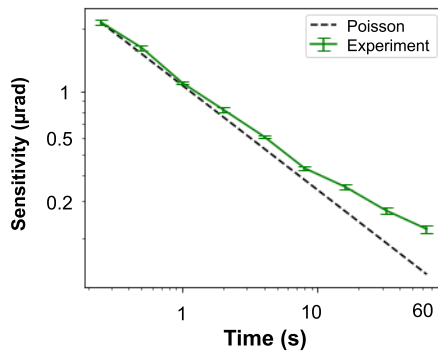
The angular sensitivity depends on the exposure time and closely follows the trend expected from the Poisson statistics, proportional to the power of  $-1/2$  (Table 1 and Fig. 3). This indicates that the main limitation in the phase retrieval process is photon statistics. The measured angular sensitivity starts departing from a perfect quantum-limited system for integration times approaching  $10\ \text{s}$ . This is due to environmental instabilities, including temperature drifts and vibrations, which become noticeable only with longer exposures. The integrated phase images of the sensitivity phantom are presented in Fig. 2(e). Smaller details emerge from the background noise as the exposure time is increased. We report submicroradian sensitivities starting at  $2\ \text{s}$  of exposure time and down to a minimum of  $220 \pm 10\ \text{nrad}$  with  $64\ \text{s}$  per frame. These values are obtained with a single-exposure image, thus with a resolution limited by the modulator pitch at  $50\ \mu\text{m}$ . With the methods described earlier, the resolution can be increased up to approximately  $16\ \mu\text{m}$  while maintaining the same angular sensitivity and increasing the total exposure time. The angular sensitivity with the Hamamatsu flat panel was slightly worse,  $(\sigma(\alpha_x), \sigma(\alpha_y)) = (1.96 \pm 0.05, 2.10 \pm 0.05)\ \mu\text{rad}$  and  $(\sigma(\alpha_x), \sigma(\alpha_y)) = (1.31 \pm 0.04, 1.41 \pm 0.02)\ \mu\text{rad}$  for  $1\ \text{s}$  and  $2\ \text{s}$  exposure times, respectively. However, the field of view was extended to  $28\ \text{mm} \times 28\ \text{mm}$  from the  $3.2\ \text{mm} \times 3.2\ \text{mm}$  achievable with the MerlinX. Many factors contribute to defining the angular sensitivity of a given system's configuration, including detection efficiency, PSF, and stability during exposure. The development of a comprehensive model for angular sensitivity is underway and beyond the scope of this work. To position our system in the landscape of existing solutions for lab-based XPC $\mu$ T, we report in Table 2 a summary of imaging system parameters from the literature, including source power, spatial resolution, system dimensions, and sensitivity. In comparison with EI and the first GBI systems, our approach achieves comparable angular sensitivity



**Fig. 2. System characterisation and benchmarking.** (a) Resolution and (c) accuracy of phase retrieval, as a function of sampling, in images of the monodisperse soda-lime glass microspheres on Kapton substrate and the PMMA calibration sphere, respectively; (a) the ability to visualize small details depends critically on a fine sampling and is mainly defined by the width aperture in the modulator. (b) The MTF matches well a real-space full width at half-maximum of  $16\ \mu\text{m}$ . (c) Phase is retrieved accurately in all cases, with higher noise linked to coarser sampling. This can also be seen in the (d) line profiles plot, where the phase shifts retrieved in the four experimental cases are compared to the theoretical phase shift. (e) Images of the angular sensitivity phantom showing microspheres and air bubbles embedded in wax in the upper half, and polyethylene foam in the lower half. Longer exposure times lead to better signal-to-noise ratios. For example, details in the foam and small void inclusions (indicated by arrows) become increasingly more visible. Exposures as short as  $250\ \text{ms}$  are sufficient for robust phase integration.

**Table 1. System Angular Sensitivity for Different Exposure Times, MerlinX Detector, and 50  $\mu\text{m}$ -pitch Modulator**

| Exp Time (s) | $\sigma(\alpha_x)(\mu\text{rad})$ | $\sigma(\alpha_y)(\mu\text{rad})$ |
|--------------|-----------------------------------|-----------------------------------|
| 0.25         | $2.14 \pm 0.05$                   | $2.33 \pm 0.07$                   |
| 0.5          | $1.62 \pm 0.04$                   | $1.66 \pm 0.03$                   |
| 1            | $1.10 \pm 0.02$                   | $1.19 \pm 0.03$                   |
| 2            | $0.82 \pm 0.02$                   | $0.85 \pm 0.02$                   |
| 4            | $0.61 \pm 0.01$                   | $0.65 \pm 0.01$                   |
| 8            | $0.43 \pm 0.01$                   | $0.46 \pm 0.01$                   |
| 16           | $0.35 \pm 0.01$                   | $0.34 \pm 0.01$                   |
| 32           | $0.27 \pm 0.01$                   | $0.31 \pm 0.01$                   |
| 64           | $0.22 \pm 0.01$                   | $0.22 \pm 0.01$                   |

**Fig. 3.** System angular sensitivity trend compared to quantum-limited ideal system, MerlinX detector, and 50  $\mu\text{m}$ -pitch modulator.

with a low-power source. The highest sensitivity was achieved with GBI [51] and the most powerful x-ray source, at the lowest spatial resolution. A more recent lab-based implementation of GBI [52] achieved high sensitivity at high resolution, and required fine-pitch gratings with a high aspect ratio. SBI [15] also reports high sensitivity and requires a large footprint and specialized source technology.

Tomographic reconstructions of  $\mu$  and  $\delta$  of the multimaterial phantom are presented in Figs. 4(a) and 4(b). The lower noise of phase tomography is apparent. This can be seen quantitatively in the histograms in panel 4(c), where the values extracted from the boxes highlighted in colors are compared. Phase contrast allows for a better separation of PP and PS with respect to attenuation contrast, and the simultaneous availability of both contrast channels improves material separation even further. Reconstruction artifacts, running vertically across both coronal planes in  $\mu$  and  $\delta$  images, are visible. They are linked to ring artifacts visible in the

transverse plane slices, which were not correct for with dedicated filters. These artifacts were excluded from the regions of interest used for quantitative analysis. Measured values are compared against theoretically expected ones [53] in Table 3. Effective energies vary slightly for  $\delta$  and  $\mu$  as expected [54]; however, the range of values is very close to the mean energy of the x-ray spectrum (15.6 keV). The contrast-to-noise ratio (CNR) is calculated as

$$\text{CNR} = \frac{\mu_m - \mu_{\text{air}}}{\sigma_{\text{air}}}, \quad (10)$$

where  $\mu_m$  is the linear attenuation coefficient of each material and  $\sigma_{\text{air}}$  is the standard deviation of the background. An analogous formula is used for  $\delta$ . CNRs were found to be substantially higher for phase tomography.

Lab-XPC $\mu\text{T}$  of the animal-derived small organs are presented in Fig. 5. The volume rendering and coronal, longitudinal, and axial slices of both samples are shown. Access to the full volume provides structural information of the specimens, which are represented with isotropic spatial resolution of approximately 16  $\mu\text{m}$ .

For the piglet esophagus [Figs. 5(a)–5(c)], we identified five different tissue layers in the phase reconstructions as labeled in the images: (1) epithelium, (2) lamina propria, (3) submucosa, (4) inner circular muscular layer, and (5) longitudinal outer muscular layer. These tissue layers are poorly, if at all, visible in the attenuation-contrast reconstructions. Figure 5(a) reports the same principle previously shown for material identification in Fig. 4, now applied to three small volumes located in different tissue layers. Increased separation can be observed in phase contrast ( $\delta$ ), and the simultaneous availability of both  $\mu$  and  $\delta$  representations vastly improves the ability to separate the layers. For the rat heart [Figs. 5(d) and 5(e)], lab-XPC $\mu\text{T}$  allowed to visualize the orientation of microfibrils in the muscle bundles and to identify the following structures: the left pulmonary vein (LPV), the aorta, the aortic valve (AV), the aortic arch (AA), the mitral valve (MV), the left ventricle (LV), the right ventricle (RV), the papillary muscles (PMs), the right atrium (RA), and the caudal vena cava (CVC). We note the presence of an iron-rich blood clot (BC) appearing brighter within the RA. The insets in the axial slice show the circumferentially oriented fibers in the mid-miocardium (line-like structures) and the longitudinally oriented fibers closer to the outer epicardium wall (point-like structures). The tomography data sets were acquired in a step-and-shoot fashion, which carried overheads. Without optimization, the total acquisition times were in the range of approximately 64 h. This mismatch is only due to a need for optimizing the sequences of positioning and detector

**Table 2. Comparison of Laboratory-based XPC $\mu\text{T}$  Systems in the Literature**

| Reference                         | Technique | Resolution               | Sensitivity       | Scan Time (s) | X-ray Spot Size                | Source Power | Dimension |
|-----------------------------------|-----------|--------------------------|-------------------|---------------|--------------------------------|--------------|-----------|
| Diemoz <i>et al.</i> [47]         | EI        | 12 or 66.8 $\mu\text{m}$ | 270 nrad          | 112 or 14 s   | 70 $\mu\text{m}$               | 875 W        | 200 cm    |
| Havariyoun <i>et al.</i> [48]     | EI        | 10 or 79 $\mu\text{m}$   | 230 nrad          | 384 or 24 s   | 70 $\mu\text{m}$               | 400 W        | 100 cm    |
| Revol <i>et al.</i> [49]          | GBI       | 104 $\mu\text{m}$        | 110 nrad          | 80.4 s        | $1 \times 1 \text{ mm}^2$      | 250–1000 W   | 140 cm    |
| Thuring <i>et al.</i> [50]        | GBI       | 4.1–7.1 $\mu\text{m}$    | 250–550 nrad      | 128 s         | 5–10 $\mu\text{m}$             | 4–12 W       | 20–33 cm  |
| Birnbacher <i>et al.</i> [51]     | GBI       | 170 $\mu\text{m}$        | 5 nrad            | 275 s         | $132 \times 226 \mu\text{m}^2$ | 2.8 kW       | 230 cm    |
| Villa-Comamala <i>et al.</i> [52] | GBI       | 21.5 $\mu\text{m}$       | 45 nrad           | 250 s         | 10 $\mu\text{m}$               | 60 W         | 90.4 cm   |
| Zanette <i>et al.</i> [15]        | SBI       | 84 $\mu\text{m}$         | 240 nrad          | 300 s         | $7.8 \times 8.7 \mu\text{m}^2$ | 30 W         | 300 cm    |
| Quénot <i>et al.</i> [19]         | SBI       | 36 $\mu\text{m}$         | 5 $\mu\text{rad}$ | 600 s         | 4 $\mu\text{m}$                | -            | 53 cm     |
| Our setup with MerlinX            | 2DBT      | 15 or 50 $\mu\text{m}$   | 345 nrad          | 256 or 16 s   | 5–20 $\mu\text{m}$             | 10 W         | 70–86 cm  |

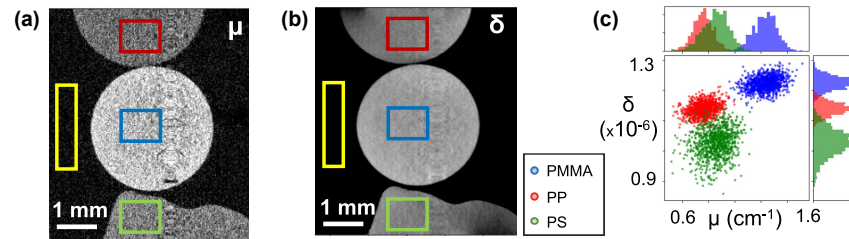


**Fig. 4. Material identification.** Longitudinal slices of (a)  $\mu$  and (b)  $\delta$  for the multimaterial phantom; (c) the ability to separate the three materials is greatly improved by the simultaneous availability of the two contrast channels.

**Table 3. Experimental and Theoretical  $\mu$  and  $\delta$  of the Phantom Materials, along with Effective Energies and CNRs Measured with Respect to the Background [yellow box in Figs. 4(a) and 4(b)]<sup>a</sup>**

| Material | $\mu_{\text{exp}}$ ( $\text{cm}^{-1}$ ) | $\mu_{\text{theo}}$ ( $\text{cm}^{-1}$ ) | $E_{\mu}$ (keV) | CNR of $\mu$ | $\delta_{\text{exp}}$ ( $\times 10^{-6}$ ) | $\delta_{\text{theo}}$ ( $\times 10^{-6}$ ) | $E_{\delta}$ (keV) | CNR of $\delta$ |
|----------|---|--|-----------------|--------------|--|---|--------------------|-----------------|
| PP       | $0.76 \pm 0.06$                         | 0.76                                     | 13              | 4.1          | $1.14 \pm 0.01$                            | 1.14  | 14                 | 31.6            |
| PMMA     | $1.23 \pm 0.06$                         | 1.23                                     | 15              | 7.1          | $1.22 \pm 0.01$                            | 1.22  | 15                 | 34.0            |
| PS       | $0.86 \pm 0.06$                         | 0.85                                     | 14              | 4.7          | $1.03 \pm 0.01$                            | 1.03  | 15                 | 28.4            |

<sup>a</sup>Good agreement is observed on both attenuation- and phase-contrast channels with expectations from theory. Phase tomography offers consistently higher CNRs.

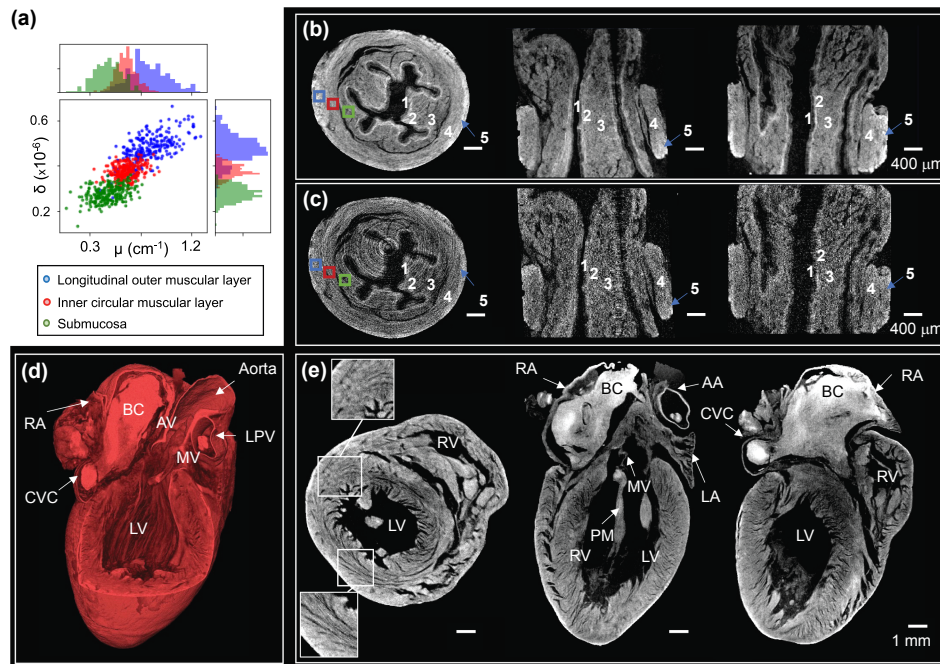


**Fig. 5. XPC $\mu$ T of (a)–(c) a piglet esophagus and (d)–(e) rat heart;** Piglet esophagus: (a)  $\mu$  and  $\delta$  histograms extracted from (b) phase contrast and (c) conventional attenuation-contrast microtomography (axial, longitudinal, and coronal slices from left to right). The numerical labels correspond to five different tissue layers that were identified in the phase-contrast channel: (1) epithelium, (2) lamina propria, (3) submucosa, (4) inner circular muscular layer, and (5) longitudinal outer muscular layer. These layers are hardly if at all visible in the images of panel (c). For the rat heart: (d) volume rendering of the phase-contrast microtomography (e) and its axial, longitudinal, and coronal slices (from left to right). The following structures were identified: the LPV, the aorta, the AV, the AA, the MV, the LV, the RV, the PMs, the RA, and the CVC. We note the presence of a BC within the RA. The circumferentially oriented fibers in the mid-miocardium and the longitudinally oriented fibers closer to the outer epicardium wall can also be observed, as highlighted by the two zoom-in insets in panel (e).

exposure. Work is currently underway to implement fly-scans for bringing the data acquisition time much closer to the actual exposure times. This work focuses on XPC $\mu$ T in a laboratory setting, and we reported only regarding the retrieval and reconstruction of two contrast channels, namely, attenuation and phase. We note, however, that the imaging system here proposed is compatible with x-ray dark-field imaging, and the approach presented here can be extended to diffuse dark-field imaging in two and three dimensions.

#### 4. CONCLUSION

We presented a compact and cost-effective system for performing XPC $\mu$ T in a laboratory setting. The system is based on a single modulator and a low-power sealed x-ray tube and is compatible with a range of readily available detectors. We report submicrometer angular sensitivity starting at 2 s of exposure time at 50  $\mu\text{m}$  spatial resolution and 32 s at 16  $\mu\text{m}$  spatial resolution, and a maximum angular sensitivity of 220 nrad in 64 s at 50  $\mu\text{m}$  spatial resolution. These results are compatible with the state of the art

and were achieved with a simple and compact setup. The proposed approach is quantitative, as validated through a phantom composed of known materials, and flexible in terms of spatial resolution and sampling. By introducing the amplitude modulator, sampling and resolution are driven by the structure of the illumination and can be tuned to the requirement of the sample by adapting the data acquisition strategy. The potential of the system for soft-tissue imaging was demonstrated on two biological specimens prepared without staining: five different tissue layers were identified in a piglet esophagus, and the orientation of microfibers within the myocardium of a rat heart was visualized. We believe that the concurrent simplicity, sensitivity, robustness, compactness, and efficiency of our approach will be instrumental in making XPC $\mu$ T more accessible and available to a wider community.

**Funding.** H2020 Marie Skłodowska-Curie Actions (843265); Royal Academy of Engineering (CiET1819/2/78, Research Fellowship Scheme); Wellcome Trust (221367/Z/20/Z); Engineering and Physical Sciences Research Council (EP/T005408/1, EP/T02593X/1, EP/T517793/1, EP/V035932/1).

**Acknowledgment.** This work was supported by the EPSRC, the Wellcome Trust, and the National Research Facility for Lab X-ray CT (NXCT) through EPSRC. A. O. is supported by the Royal Academy of Engineering under their Chair in Emerging Technologies scheme. C. K. H. is supported by the Royal Academy of Engineering under the Research Fellowship Scheme. M. F. M. G. is supported by an H2020 Marie Skłodowska Curie Action Fellowship (AmnioticID). S. S. is a UKRI EPSRC Doctoral Prize fellow.

Conceptualization, M. E.; methodology, M. E., C.N.-L., A. D., G. P. S.C., A. A.; software, C. N.-L., A. D., A. A., C. K. H.; investigation, C. N.-L., A. D., M. E.; resources, M. E., G. P. S. C., A. A., S. S., M. F. M. G., A. O.; writing, C. N.-L., M. E.; review, C. N.-L., A. D., S. S., M. F. M. G., G. P. A. A., S. C., D. B., C. K. H., A. O., M. E.; supervision, A. O., D. B., C. K. H., S. C., M. E.; funding acquisition, A. O., D. B., C. K. H., M. E.

**Disclosures.** The authors declare no conflicts of interest.

**Data availability.** Data underlying the results presented in this paper are not publicly available at this time but may be obtained from the authors upon reasonable request.

## REFERENCES

- P. J. Withers, C. Bouman, S. Carmignato, V. Cnudde, D. Grimaldi, C. K. Hagen, E. Maire, M. Manley, A. D. Plessis, and S. R. Stock, "X-ray computed tomography," *Nat. Rev. Methods Primers* **1**, 18 (2021).
- S. R. Stock, "Recent advances in x-ray microtomography applied to materials," *Int. Mater. Rev.* **53**, 129–181 (2008).
- E. Maire and P. J. Withers, "Quantitative x-ray tomography," *Int. Mater. Rev.* **59**, 1–43 (2013).
- D. Paganin, *Coherent X-Ray Optics* (Oxford University, 2006).
- T. J. Davis, D. Gao, T. E. Gureyev, A. W. Stevenson, and S. W. Wilkins, "Phase-contrast imaging of weakly absorbing materials using hard x-rays," *Nature* **373**, 595–598 (1995).
- S. W. Wilkins, T. E. Gureyev, D. Gao, A. Pogany, and A. W. Stevenson, "Phase-contrast imaging using polychromatic hard x-rays," *Nature* **384**, 335–338 (1996).
- F. Pfeiffer, T. Weitkamp, O. Bunk, and C. David, "Phase retrieval and differential phase-contrast imaging with low-brilliance X-ray sources," *Nat. Phys.* **2**, 258–261 (2006).
- M. Bech, T. H. Jensen, R. Feidenhans, O. Bunk, C. David, and F. Pfeiffer, "Soft-tissue phase-contrast tomography with an x-ray tube source," *Phys. Med. Biol.* **54**, 2747–2753 (2009).
- J. Herzen, T. Donath, F. Pfeiffer, O. Bunk, C. Padeste, F. Beckmann, A. Schreyer, and C. David, "Quantitative phase-contrast tomography of a liquid phantom using a conventional X-ray tube source," *Opt. Express* **17**, 10010 (2009).
- A. Olivo and R. Speller, "A coded-aperture technique allowing X-ray phase contrast imaging with conventional sources," *Appl. Phys. Lett.* **91**, 074106 (2007).
- C. K. Hagen, P. R. T. Munro, M. Endrizzi, P. C. Diemoz, and A. Olivo, "Low-dose phase contrast tomography with conventional X-ray sources," *Med. Phys.* **41**, 070701 (2014).
- H. H. Wen, E. E. Bennett, R. Kopace, A. F. Stein, and V. Pai, "Single-shot X-ray differential phase-contrast and diffraction imaging using two-dimensional transmission gratings," *Opt. Lett.* **35**, 1932–1934 (2010).
- O. Hemberg, M. Otendal, and H. M. Hertz, "Liquid-metal-jet anode electron-impact X-ray source," *Appl. Phys. Lett.* **83**, 1483–1485 (2003).
- H. Miao, A. Panna, A. A. Gomella, E. E. Bennett, S. Znati, L. Chen, and H. Wen, "A universal moiré effect and application in X-ray phase-contrast imaging," *Nat. Phys.* **12**, 830–834 (2016).
- I. Zanette, T. Zhou, A. Burvall, U. Lundström, D. Larsson, M. Zdora, P. Thibault, F. Pfeiffer, and H. Hertz, "Speckle-based X-ray phase-contrast and dark-field imaging with a laboratory source," *Phys. Rev. Lett.* **112**, 253903 (2014).
- I. Zanette, M.-C. Zdora, T. Zhou, A. Burvall, D. H. Larsson, P. Thibault, H. M. Hertz, and F. Pfeiffer, "X-ray microtomography using correlation of near-field speckles for material characterization," *Proc. Natl. Acad. Sci. USA* **112**, 12569–12573 (2015).
- T. Zhou, F. Yang, R. Kaufmann, and H. Wang, "Applications of laboratory-based phase-contrast imaging using speckle tracking technique towards high energy X-rays," *J. Imaging* **4**, 69 (2018).
- H. Wang, Y. Kashyap, and K. Sawhney, "From synchrotron radiation to lab source: advanced speckle-based X-ray imaging using abrasive paper," *Sci. Rep.* **6**, 20476 (2016).
- L. Quénot, H. Rougé-Labriet, S. Bohic, S. Berujon, and E. Brun, "Implicit tracking approach for X-ray phase-contrast imaging with a random mask and a conventional system," *Optica* **8**, 1412–1415 (2021).
- S. W. Wilkins, Y. I. Nesterets, T. E. Gureyev, S. C. Mayo, A. Pogany, and A. W. Stevenson, "On the evolution and relative merits of hard X-ray phase-contrast imaging methods," *Philos. Trans. R Soc. A* **372**, 20130021 (2014).
- A. Bravin, P. Coan, and P. Suortti, "X-ray phase-contrast imaging: from pre-clinical applications towards clinics," *Phys. Med. Biol.* **58**, R1–R35 (2012).
- R. Hanke, T. Fuchs, M. Salamon, and S. Zabler, "X-ray microtomography for materials characterization," in *Materials Characterization Using Nondestructive Evaluation (NDE) Methods* (Elsevier, 2016), pp. 45–79.
- A. Momose, "X-ray phase imaging reaching clinical uses," *Phys. Med.* **79**, 93–102 (2020).
- S. Tao, C. He, X. Hao, C. Kuang, and X. Liu, "Principles of different X-ray phase-contrast imaging: a review," *Appl. Sci.* **11**, 2971 (2021).
- L. Birnbacher, E.-M. Braig, D. Pfeiffer, F. Pfeiffer, and J. Herzen, "Quantitative X-ray phase contrast computed tomography with grating interferometry," *Eur. J. Nucl. Med. Mol. Imaging* **48**, 4171–4188 (2021).
- B. Müller, S. R. Stock, G. Wang, and J. G. Brankov, "Special section guest editorial: hard X-ray tomography with micrometer resolution," *J. Med. Imaging* **9**, 031501 (2022).
- A. Velroyen, A. Yaroshenko, D. Hahn, A. Fehringer, A. Tapfer, M. Müller, P. Noël, B. Pauwels, A. Sasov, A. Yildirim, O. Eickelberg, K. Hellbach, S. Auweter, F. Meinel, M. Reiser, M. Bech, and F. Pfeiffer, "Grating-based X-ray dark-field computed tomography of living mice," *EBioMedicine* **2**, 1500–1506 (2015).
- R. P. Murrie, F. Werdiger, M. Donnelly, Y. W. Lin, R. P. Carnibella, C. R. Samarage, I. Pinar, M. Preissner, J. Wang, J. Li, K. S. Morgan, D. W. Parsons, S. Dubsy, and A. Fouras, "Real-time in vivo imaging of regional lung function in a mouse model of cystic fibrosis on a laboratory X-ray source," *Sci. Rep.* **10**, 447 (2020).
- L. Massimi, T. Suaris, C. K. Hagen, M. Endrizzi, P. R. T. Munro, G. Havariyou, P. M. S. Hawker, B. Smit, A. Astolfo, O. J. Larkin, R. M. Waltham, Z. Shah, S. W. Duffy, R. L. Nelan, A. Peel, J. L. Jones, I. G. Haig, D. Bate, and A. Olivo, "Detection of involved margins in breast specimens with X-ray phase-contrast computed tomography," *Sci. Rep.* **11**, 3663 (2021).
- M. Reichardt, M. Töpperwien, A. Khan, F. Alves, and T. Salditt, "Fiber orientation in a whole mouse heart reconstructed by laboratory phase-contrast micro-CT," *J. Med. Imaging* **7**, 1 (2020).
- S. Savvidis, M. F. Gerli, M. Pellegrini, L. Massimi, C. K. Hagen, M. Endrizzi, A. Atzeni, O. K. Ogunbiyi, M. Turmaine, E. S. Smith, C. Fagiani, G. Selmin, L. Urbani, N. Durkin, S. Shibuya, P. D. Coppi, and A. Olivo,

- "Monitoring tissue engineered constructs and protocols with laboratory-based X-ray phase contrast tomography," *Acta Biomater.* **141**, 290–299 (2022).
32. M. Töpperwien, M. Krenkel, D. Vincenz, F. Stöber, A. M. Oelschlegel, J. Goldschmidt, and T. Salditt, "Three-dimensional mouse brain cytoarchitecture revealed by laboratory-based X-ray phase-contrast tomography," *Sci. Rep.* **7**, 42847 (2017).
33. M. Willner, M. Viermetz, M. Marschner, K. Scherer, C. Braun, A. Fingerle, P. Noël, E. Rummeny, F. Pfeiffer, and J. Herzen, "Quantitative three-dimensional imaging of lipid, protein, and water contents via X-ray phase-contrast tomography," *PLOS ONE* **11**, e0151889 (2016).
34. T. Weber, G. Pelzer, J. Rieger, A. Ritter, and G. Anton, "Report of improved performance in Talbot-Lau phase-contrast computed tomography," *Med. Phys.* **42**, 2892–2896 (2015).
35. X. Ji, R. Zhang, K. Li, and G.-H. Chen, "Dual energy differential phase contrast CT (DE-DPC-CT) imaging," *IEEE Trans. Med. Imaging* **39**, 3278–3289 (2020).
36. D. Shoukroun, L. Massimi, F. Iacoviello, M. Endrizzi, D. Bate, A. Olivo, and P. Fromme, "Enhanced composite plate impact damage detection and characterisation using X-ray refraction and scattering contrast combined with ultrasonic imaging," *Composites B* **181**, 107579 (2020).
37. F. A. Vittoria, G. K. N. Kallon, D. Basta, P. C. Diemoz, I. K. Robinson, A. Olivo, and M. Endrizzi, "Beam tracking approach for single-shot retrieval of absorption, refraction, and dark-field signals with laboratory X-ray sources," *Appl. Phys. Lett.* **106**, 224102 (2015).
38. E. Dreier, A. Bergamaschi, G. K. Kallon, R. Brönnimann, U. L. Olsen, A. Olivo, and M. Endrizzi, "Tracking based, high-resolution single-shot multimodal X-ray imaging in the laboratory enabled by the sub-pixel resolution capabilities of the MÖNCH detector," *Appl. Phys. Lett.* **117**, 264101 (2020).
39. M. D. de Jonge, B. Hornberger, C. Holzner, D. Legnini, D. Paterson, I. McNulty, C. Jacobsen, and S. Vogt, "Quantitative phase imaging with a scanning transmission X-ray microscope," *Phys. Rev. Lett.* **100**, 163902 (2008).
40. P. C. Diemoz, F. A. Vittoria, and A. Olivo, "Spatial resolution of edge illumination X-ray phase-contrast imaging," *Opt. Express* **22**, 15514–15529 (2014).
41. C. K. Hagen, F. A. Vittoria, M. Endrizzi, and A. Olivo, "Theoretical framework for spatial resolution in edge-illumination X-ray tomography," *Phys. Rev. Appl.* **10**, 054050 (2018).
42. J. R. Fienup, M. Guizar-Sicairos, and S. T. Thurman, "Efficient subpixel image registration algorithms," *Opt. Lett.* **33**, 156–158 (2008).
43. C. Kottler, C. David, F. Pfeiffer, and O. Bunk, "A two-directional approach for grating based differential phase contrast imaging using hard X-rays," *Opt. Express* **15**, 1175–1181 (2007).
44. P. Modregger, B. R. Pinzer, T. Thüring, S. Rutishauser, C. David, and M. Stampanoni, "Sensitivity of X-ray grating interferometry," *Opt. Express* **19**, 18324–18338 (2011).
45. W. van Aarle, W. J. Palenstijn, J. De Beenhouwer, T. Altantzis, S. Bals, K. J. Batenburg, and J. Sijbers, "The ASTRA toolbox: a platform for advanced algorithm development in electron tomography," *Ultramicroscopy* **157**, 35–47 (2015).
46. C. Navarrete-León, A. Doherty, A. Astolfo, C. K. Hagen, P. Munro, A. Olivo, and M. Endrizzi, "Two-directional beam-tracking for phase-sensitive X-ray tomography with laboratory sources," 15th International Conference on X-ray Microscopy (XRM), Hsinchu, Taiwan (19–24 June 2022).
47. P. C. Diemoz, C. K. Hagen, M. Endrizzi, and A. Olivo, "Sensitivity of laboratory based implementations of edge illumination X-ray phase-contrast imaging," *Appl. Phys. Lett.* **103**, 244104 (2013).
48. G. Havariryoun, F. A. Vittoria, C. K. Hagen, *et al.*, "A compact system for intraoperative specimen imaging based on edge illumination X-ray phase contrast," *Phys. Med. Biol.* **64**, 235005 (2019).
49. V. Revol, C. Kottler, R. Kaufmann, U. Straumann, and C. Urban, "Noise analysis of grating-based X-ray differential phase contrast imaging," *Rev. Sci. Instrum.* **81**, 073709 (2010).
50. T. Thüring, S. Hämmerle, S. Weiss, J. Nüesch, J. Meiser, J. Mohr, C. David, and M. Stampanoni, "Compact hard X-ray grating interferometry for table top phase contrast micro CT," *Proc. SPIE* **8668**, 293–299 (2013).
51. L. Birnbacher, M. Willner, A. Velroyen, M. Marschner, A. Hipp, J. Meiser, F. Koch, T. Schröter, D. Kunka, J. Mohr, F. Pfeiffer, and J. Herzen, "Experimental realisation of high-sensitivity laboratory X-ray grating-based phase-contrast computed tomography," *Sci. Rep.* **6**, 24022 (2016).
52. J. Vila-Comamala, L. Romano, K. Jefimovs, H. Dejea, A. Bonnin, A. C. Cook, I. Planinc, M. Cikes, Z. Wang, and M. Stampanoni, "High sensitivity X-ray phase contrast imaging by laboratory grating-based interferometry at high Talbot order geometry," *Opt. Express* **29**, 2049–2064 (2021).
53. B. L. Henke, E. M. Gullikson, and J. C. Davis, "X-ray interactions: photoabsorption, scattering, transmission, and reflection at  $e = 50$ –30,000 eV,  $z = 1$ –92," *At. Data Nucl. Data Tables* **54**, 181–342 (1993).
54. P. R. Munro and A. Olivo, "X-ray phase-contrast imaging with polychromatic sources and the concept of effective energy," *Phys. Rev. A* **87**, 053838 (2013).